Subduction initiation at an oceanic transform fault experiencing compression: Role of the fault structure and of the brittle-ductile transition depth

Diane Arcay, Sarah Abecassis, Serge Lallemand

▶ **To cite this version:**

Diane Arcay, Sarah Abecassis, Serge Lallemand. Subduction initiation at an oceanic transform fault experiencing compression: Role of the fault structure and of the brittle-ductile transition depth. Earth and Planetary Science Letters, 2023, 618, pp.118272. 10.1016/j.epsl.2023.118272 . hal-04176730

HAL Id: hal-04176730
https://hal.science/hal-04176730v1

Submitted on 22 Nov 2023

HAL is a multi-disciplinary open access archive for the deposit and dissemination of scientific research documents, whether they are published or not. The documents may come from teaching and research institutions in France or abroad, or from public or private research centers.

L'archive ouverte pluridisciplinaire **HAL**, est destinée au dépôt et à la diffusion de documents scientifiques de niveau recherche, publiés ou non, émanant des établissements d'enseignement et de recherche français ou étrangers, des laboratoires publics ou privés.

Graphical Abstract

Subduction initiation at an oceanic transform fault experiencing compression: Role of the fault structure and of the brittle-ductile transition depth

D. Arcay, S. Abecassis, S. Lallemand

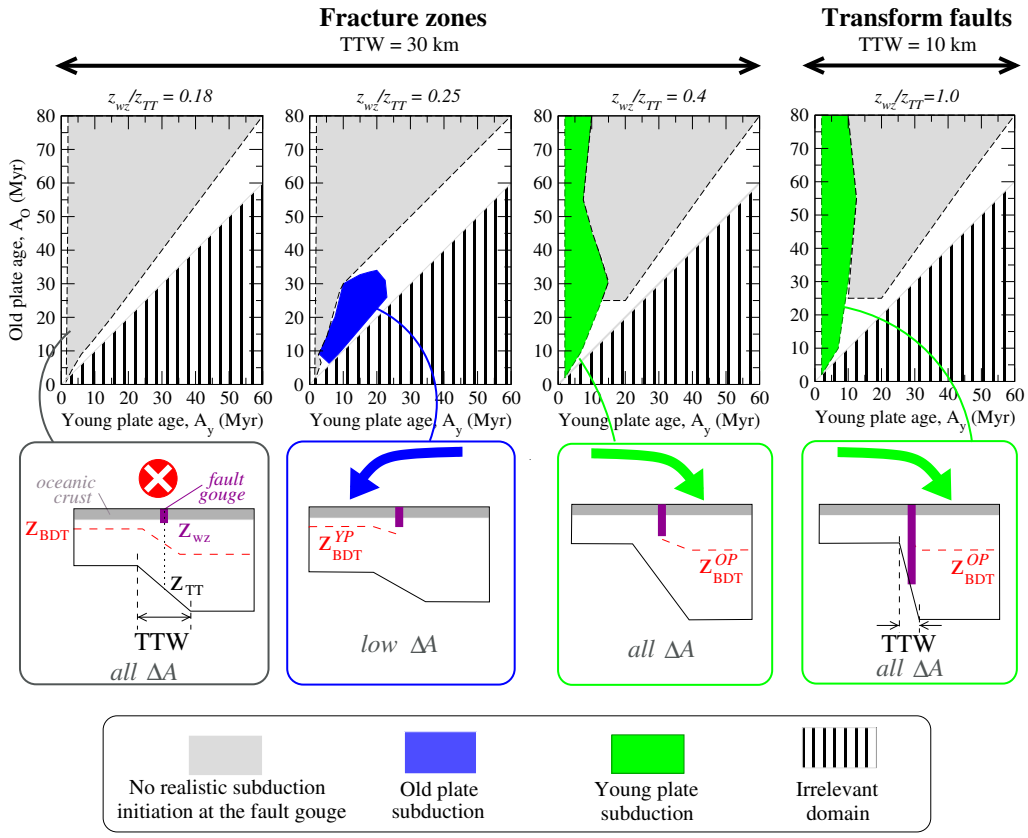

Highlights

- The initial fault gouge depth controls the subduction initiation success and polarity
- The setup of an active transform fault only yields the thin plate underthrusting
- The thicker plate subduction is restricted to old fracture zone setups.
- No subduction initiation if at least one of the 2 plates is older than 30 Myr.
- The numerical results agree with Cenozoic subduction initiations at transform faults.

Arcay, Abecassis, & Lallemand (2023). Subduction initiation at an oceanic transform fault experiencing compression: Role of the fault structure and of the brittle-ductile transition depth. Earth and Planetary Science Letters, 618, 118272.

Subduction initiation at an oceanic transform fault experiencing compression: Role of the fault structure and of the brittle-ductile transition depth

D. Arcay, S. Abecassis, S. Lallemand

[a]*Geosciences Montpellier, Univ. of Montpellier, CNRS, Montpellier, France*

Abstract

It has recently been shown that among the subduction zones initiated in the Cenozoic era, the subducting oceanic lithosphere could have any age, and was as often older than the overriding plate as younger than it. To try to explain this observation, we consider the simple setup of an oceanic transform fault and perform 2D thermomechanical experiments by applying the same convergence velocity on the two adjacent plates. We combine a non-Newtonian viscous rheology and a pseudo-brittle behavior. We focus on the influence of the fault structure at convergence onset, by testing the effects of the fault gouge depth, z_{wz}, and of the width of the thermal transition between the lithospheres, which allows for mimicking the settings of a transform fault as well as of an old fracture zone. We investigate large ranges of plate age and of plate age offset. In most of our experiments, the mode of convergence accommodation is basically a function of the gouge depth, z_{wz}, that we compare to the mean of the 2 plate thicknesses. We observe three main behaviors: (1) failure of subduction initiation if z_{wz} is shallow, i.e., $\lesssim$15% of the mean depth of the 2 plate bottoms if the age offset scaled by the younger age is very low ($\lesssim$1) or $\lesssim$30% otherwise, (2) old plate subduction, that is best favored for ratios z_{wz}/z_{TT} ~0.25 and for low offsets in relative plate ages, and (3) young plate subduction if z_{wz} is quite deep ($\gtrsim$40%), whatever the age offset. The thermal transition width only has a second-order effect, that facilitates subduction initiation when the transition is wide. Compressive forces are overshooting reasonable thresholds ($\gtrsim 10^{13}$ N/m) if at least one of the two plates is older than ~30 Myr. The success of a young plate subduction and, to a lesser extent, of an old plate subduction, can be predicted by comparing z_{wz} at convergence onset to the depth of the brittle-ductile transition inside the future upper plate. The subduction success and polarity depend on the possibility to form a low shear stress plane. We predict that only the young plate subduction can initiate at an active transform fault, while the old plate subduction is restricted to the setup of an old fracture zone separating two lithospheres with a small age offset scaled by the younger age. The significant predominance in our modeling of the thin plate underthrusting results from the strong influence of the plate strength contrast when lithospheres are stiff. Our experimental results are consistent with the recent records of subduction initiation at the Mussau and Hjort Trenches, as well as at the Gagua ridge (W Pacific).

Keywords:
subduction initiation, oceanic transform fault, numerical simulations

1. Introduction

How does subduction initiation operate on Earth under present-day conditions? It has been suggested that the incoming plate had to be strongly negatively buoyant, which would further promote the future subduction zone self-sustainment (e.g., Hall and Gurnis, 2003; Gurnis et al., 2004). In that respect, an incipient subduction zone where the subducting plate is the thinner and less dense of the two adjacent lithospheres as been deemed as 'anomalous' or 'atypical' (Zhang et al., 2021; Wang et al., 2022a). Nevertheless, a young lithosphere is warm, and likely to deform more easily than an old one. The question is meaningful, because when considering all the Cenozoic subduction initiation events, in half the cases the nascent incoming plate was younger than 40 Myr (Lallemand and Arcay, 2021), thence hardly denser than the underlying asthenosphere (Oxburgh and Parmentier, 1977). To try to understand the origin of this paradox, an oceanic transform fault undergoing compression represents a relatively simple and hence appropriate geological setting to investigate.

In such a setup, Zhang et al. (2021) showed that the plate strength is decisive. Soft plates favor the subduction of the denser lithosphere, if the density offset is sufficient. In contrast, for a high plastic resistance, the plate strength offset has a major impact and leads to the underthrusting of the thinner plate. This is when the two converging plates are assumed to behave as a mantle layer. Boutelier and Beckett (2018) showed that the interplate contact structure could control the subduction zone polarity, which underlines the influence of the fault mechanical structure. From this point of view, the cases of an active transform fault and of a fracture zone should be differentiated. The fault thermal structure may depend on the amount of heat advection, driven by the strike-slip motion, which should affect the structure and width of the thermal transition between the two lithospheres (Behn et al., 2007). Furthermore, the depth extent of the fault gouge might be a function of the strike-slip record. To our knowledge, the potential effects of the initial fault structure on subduction initiation have never been carefully investigated, which we propose to do by performing

thermo-mechanical experiments. We studied earlier the conditions allowing for the gravitational lithospheric instability at a transform fault without any horizontal forcing ('spontaneous subduction', Arcay et al., 2020). We now focus on the processes controlling the success or failure of subduction initiation when convergence is imposed far away from the transform fault.

We present an extensive modeling study, investigating large ranges of plate age and of fault structure to identify the main factors leading to a successful subduction initiation, and determining the subduction polarity. The initial fault gouge depth appears as a key parameter regarding the subduction initiation fate (achievement or failure), but also, when successful, the underthrusting polarity. Our results suggest that the transform fault setting promotes the initiation of the thinner plate underthrusting, whatever the considered plate age offset. The subduction of the thicker and older plate is restricted in our modeling to the setup of quite old fracture zones that separate two lithospheres with a low age offset. We finally compare our results to present-day subduction initiation at Mussau and Hjort trenches, but also to the geological records at the Gagua Ridge.

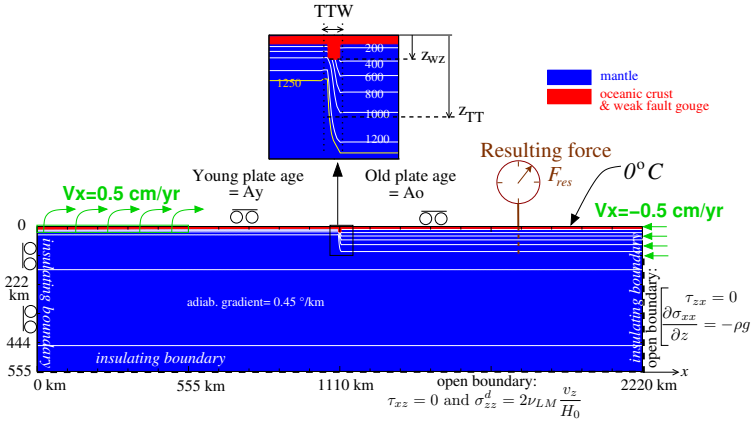

Figure 1: Boundary conditions and initial thermal and compositional fields. The initiation conditions are illustrated with simulation N6c (5vs80 Myr, TTW=10 km and z_{wz} = 21 km. The isotherms are depicted every 200^o C (white lines), apart the 1250^o C displayed in yellow in the upper insert. Mechanical open bottom boundary: the viscosity of the fictitious lower mantle ν_{LM} is set to 30 times the viscosity just ahead the bottom box, ν_{BB}. Note that in Fig. 2, 3 and 8 to 6, the younger plate will always be located on the left-hand side of the fault gouge, as shown here.

2. Model set-up

2.1. *Boundary conditions, initial state, rheology and numerical resolution*

We solve, in the extended Boussinesq approximation, the equations of conservation of mass, momentum, and energy, on a 2D large simulation box (2220 km wide and 555 km high, Fig. 1), assuming incompressibility except for the thermal expansion term in the momentum equation. Dissipation energy, adiabatic heating, and uniform heat production are included in the equation of energy conservation. The composition field (oceanic crust or mantle) is tracked using active Lagrangian markers, with specific density and rheology, that are advected with the velocity field.

The lithospheres are covered by a horizontal layer of oceanic crust, 8.3 km thick. The weak zone simulating the transform fault/fracture zone is initially located at the middle of the box (Fig. 1), simply assumed to be vertical and made of oceanic crust. The weak zone width is set to 8.3 km, which is a reasonable value for oceanic transform faults (Ren et al., 2022). The remaining part of the simulation box is filled with a mantle composition.

The simulation box is heated by a uniform and constant radiogenic source (Table S1 in the Supplementary Material). The thermal structures of each of the two lithospheres located on both sides of the weak zone result from a preliminary run of lithospheric cooling, computed with the same thermal boundary conditions as those of subduction initiation experiments, in a closed box the sides of which are set to free slip. At the start of the preliminary experiments, the asthenospheric thermal field (adiabatic gradient) is extended up to the box surface. The thermal structure of a lithosphere with a given age is picked from the cooling run at the corresponding selected time. The assembling of the two lithospheres forming the transform fault is explained in section 2.2.

The subduction initiation experiments are performed by imposing the same convergence velocity (0.5 cm/yr) on both plates far away from the vertical weak zone. The left-hand and young lithosphere is pushed from the surface up to 15 km depth over a 555 km length, while the convergence is imposed along the right-hand side of the old plate, up to its base (depth of the 1200^oC isotherm, Fig. 1). The horizontal flows are free along the remaining open right-hand side. We verify that the asymmetry of kinematic conditions does not affect the results, by reversing the two plates'location in a first set of experiments (28 simulations varying the age contrast and the fault structures, Abecassis et al., 2015). To simplify, we choose to neglect active mantle flows as a possible engine driving subduction initiation (e.g., Baes et al., 2018; Lallemand and Arcay, 2021). Along the open bottom of the simulation box, a resistance is imposed against vertical flows, mimicking the higher viscosity of a fictitious lower mantle (Ribe and Christensen, 1994). Other mechanical and thermal boundary conditions are depicted in Fig 1. The fixed thermo-mechanical parameters are listed in the supplementary Table S1.

We combine a non-Newtonian ductile creep and a pseudo-brittle behavior (Arcay et al., 2020). The non-Newtonian viscosity, ν_d, is temperature-, pressure-, composition- and strain rate-dependent, following an Arrhenius law. The simulated mantle approximately behaves as wet olivine (dunite, Chopra and Paterson, 1981), while the ductile strength of the modeled oceanic crust is close to the one of a wet quartzite and of a dry quartzite at low and high temperature, respectively (Gleason and Tullis, 1995; Ranalli and Murphy, 1987, Table S1 in the supple. mat.). A yield stress that linearly increases with depth, τ_y, is used to define a pseudo-brittle viscosity, ν_b, by using a reference strain rate, $\dot{\varepsilon}_{ref}$: $\nu_b = \tau_y(\dot{\varepsilon}/\dot{\varepsilon}_{ref})^{1/n_p} \times \dot{\varepsilon}^{-1}$, where n_p is a high exponent. The yield stress writes as: $\tau_y = C_0 + \gamma(C)P$,

where C_0 is the cohesion, P is the lithostatic pressure, and γ is the yield stress increase with depth depending on composition C. Note that γ is not the friction coefficient linking the shear and the normal stresses, though γ is related to it (Turcotte and Schubert, 1982; Arcay et al., 2020). The effective viscosity ν_{eff} is the harmonic mean of the latter two viscosities: $\nu_{eff} = (\nu_d^{-1} + \nu_b^{-1})^{-1}$. The crust rheology is significantly weaker than the mantle one both in the ductile and in the brittle realms (Table S1).

Simulations are performed using the finite element Eulerian code solving the thermo-mechanical equations on a non-deforming grid (Christensen, 1992). The rectangular numerical mesh, made of 503×118 elements in the horizontal and vertical directions, is refined in a domain centered on the initial weak zone, between x =789 and 1378 km, where the x- and z-spacings are 1.73 and 1.66 km, respectively. Outside the high resolution area, the maximum x- and z-spacings are 10.5 and 10.1 km. The density of compositional markers is uniform (~2.63 km^{-2}) and verifies a minimum of 7 markers in the smallest mesh cell (Arcay, 2017).

2.2. Simulation of the fault structure and investigated parameters

The young and old lithospheres (ages A_y and A_o) are set on the left-hand and right-hand sides, respectively, of the box. We explore age offsets varying from 3 to 75 Myr, in agreement with the range of age contrast observed at oceanic transform faults (Ren et al., 2022). The investigated lithosphere ages A_y and A_o are encompassed between 2 and 55 Myr, and 5 to 80 Myr, respectively, and combined in a dozen pairs of plate ages to explore a large variability of the tectonic framework. We systematically investigate the effects of: (1) the plate age pair, (2) the fault gouge depth, and (3) the structure of the transition zone between the plates, as explained below. This large parameter exploration allows for assessing the respective influences of parameters 1 to 3 (sections 3.1 to 3.3). We next select some experiments to decipher how subduction initiates for two geological settings, namely a fracture zone and a transform fault, by picking the parameter set that best mimics each one (section 3.4).

An inactive fracture zone may present a smooth transition between the two lithospheric thermal structures, resulting from thermal diffusion. In constrast, the horizontal diffusion across an active transform fault may be somehow offset by the strike-slip motion, depending on the slip velocity, that can be quite fast (~13 cm/yr, Siqueiros, Fornari et al., 1989) or slow (~1.4 cm/yr, Kane, Detrick Jr and Purdy, 1980). We choose to test two moderate widths of the thermal transition between the two lithospheres, 10 and 30 km, always centered on the middle of the simulation box (Fig 1). The thermal field of the thermal transition is computed by imposing at each vertical numerical node a horizontal linear increase between the temperatures of the two lithospheres. We find that this simple approximation yields a modeling of the thermal transition very similar to the one imaged and modeled by Wang et al. (2022b) at the Romanche transform fault. The equivalent 'lithospheric thickness' within the thermal transition could be related to the location of the 1250^{o}C isotherm, the depth of which strongly increases from the depth of the young lithosphere bottom to the old one. We define a mean depth, labeled z_{TT}, as the mean of the depths of the two plate bases. It gives an estimate of the depth range within the thermal transition (Fig 1).

The vertical weak zone forming the fault gouge is set in the middle of the thermal transition. How to assess its depth? As an active transform fault is a plate boundary, the weak zone forming the fault gouge is assumed to cut across the whole lithospheric thickness. Indeed, the structure of the Romanche transform fault imaged by Wang et al. (2022b) reveals that the uppermost part of the weak zone (≤15 km) may be enriched in serpentinite, while the intermediate segment (15-35 km) is mylonitic and made of hydrous peridotite. The deepest part of the weak zone is characterized by a low velocity anomaly extending down to ~60 km depth (1370^o C isotherm) probably resulting from hydrous mantle melting. Hence the weak zone depth, z_{wz} should equal z_{TT} for a transform fault. For a fracture zone, we hypothesize that the fault gouge reached a maximum depth at the end of the fault activity (defining z_{wz} at the fossilized z_{TT}), then that the subsequent conductive cooling has deepened the thermal transition beyond, rising the final z_{TT}. Therefore, we assume that $z_{wz} < z_{TT}$ for a fracture zone, the offset between these two depths being a function of the time span of the fault inactivity, which is difficult to assess. Wolfson-Schwehr and Boettcher (2019) suggest that the length of the fracture zone may be an indication of its activity duration, and could be used with the slip rate to estimate the time span since strike-slip motion stopped. We choose to vary z_{wz} between a maximum usually set to z_{TT}, and a minimum, given by the modeled Moho depth (8.3 km).

3. Results

The three main behaviors obtained in our experiments are described in the first sections. We next relate the mode of convergence to the fault structure parameters. The simulations are considered as leading to either admissible or not realistic stress levels, as a function of the tectonic force sustaining convergence at constant rate (section 3.3). We then present the simulation results regarding the respective setups of an inactive fracture zone and of an active oceanic transform fault. The simulations quoted in the main text are listed in Table 1.

3.1. Modes of convergence accommodation

3.1.1. Failure of subduction initiation at the fault zone

Simulations N2b and N5f (5vs10 Myr and 5vs55 Myr, respectively, Fig 2, row 1) are well representative of a case showing the lack of convergence localization at the weak fault zone. Convergence is first mainly accommodated by the buckling of the young plate (YP) during ~5 to ~ 8 Myr, while the velocity imposed on the old plate (OP) is progressively transmitted up to the left-hand part of the YP, at the extremity of the domain where the kinematic condition is applied (x =555 km, Fig 1). From then on, convergence is fully and continuously accommodated at this place by the shortening and sinking of the young lithosphere.

Table 1: List of the simulations quoted in the text, presented as a function of first, increasing young plate age, and, second, increasing old plate age. The first letter in the simulation labelling indicates the thermal transition width, either narrow ('N') and equals to 10 km, or wide ('W') and set to 30 km. The alphabetical tag refers to the weak zone depth at simulation start. 'No loc.': No deformation localization at the fault gouge. 'OPs': OP subduction initiation. 'YPs': YP subduction initiation. 'SOPs/SYPs.': secondary deformation localization at the fault gouge, yielding either YP or OP subduction initiation (section 3.1.4). 'Unease OPs': deformation is first partitioned between YP shortening at the left-hand kinematic condition and shortening at the fault gouge, before deformation localizes at the fault gouge and plate underthrusting becomes dominant. 'Double S': both lithospheres are simultaneously subducting. $\overline{F_{res}}^{\forall t}$ is the resulting force mean computed on the total simulation duration. 'admis.' and 'too cp': the F_{res} evolution is considered as admissible or excessively compressive, with respect to the considered threshold (see section 3.3). The complete simulation list can be found in the Supple. data (Table S1).

Run	A_y (Myr)	A_o (Myr)	$\Delta A/A_y$	z_{TT} (km)	TTW (km)	z_{wz} (km)	Result	$\overline{F_{res}}^{\forall t}$ (10^{12} N/m)	Conclusion if $F_1^{threshold}$ = 10^{13}N/m	Conclusion if $F_2^{threshold}$ = 1.5×10^{13} N/m
N1c	2	5	1.5	35.6	10	9.9	SOPs	4.5	admis.	admis.
N1d	2	5	1.5	35.6	10	11	double S	5.1	admis.	admis.
N2b	5	10	1	46.7	10	9.9	No loc.	19.8	too cp	too cp
N2d	5	10	1	46.7	10	12.3	OPs	7.4	admis.	admis.
N2g	5	10	1	46.7	10	17.2	YPs	3.6	admis.	admis.
N5f	5	55	10	67.7	10	23.3	No loc.	17.2	too cp	too cp
N5g	5	55	10	67.7	10	24.4	SYPs	12.4	too cp	too cp
N5i	5	55	10	67.7	10	26.7	YPs	6.1	admis.	admis.
N6c	5	80	15	73.2	10	21	No loc.	13.6	too cp	too cp
N7c	10	30	2	65	10	22.3	No loc.	22.8	too cp	too cp
N10c	20	30	0.5	72.2	10	12.2	OPs	9.8	too cp	too cp
N10d	20	30	0.5	72.2	10	14.1	OPs	8.5	too cp	too cp
N10e	20	30	0.5	72.2	10	16.0	OPs	8.3	too cp	admis.
N10f	20	30	0.5	72.2	10	17.9	OPs	8.7	too cp	admis.
N10g	20	30	0.5	72.2	10	26.3	OPs	10.7	too cp	too cp
W1c	2	5	1.5	35.6	30	9.8	Unease OPs	3.5	admis.	admis.
W7e	10	30	2	65	30	22.0	YPs	7.5	too cp	admis.
W10b	20	30	0.5	72.2	30	12.2	OPs	9.9	too cp	too cp
W10c	20	30	0.5	72.2	30	15.9	OPs	7.2	too cp	admis.
W10d	20	30	0.5	72.2	30	17.9	OPs	8.1	too cp	admis.
W10d2	20	30	0.5	72.2	30	17.9	OPs	8.2	too cp	admis.
W10e	20	30	0.5	72.2	30	24.0	OPs	10.4	too cp	too cp
W10f	20	30	0.5	72.2	30	25.0	YPs	13.7	too cp	too cp
W12h	55	80	0.454	100.1	30	39.3	YPs	40.2	too cp	too cp

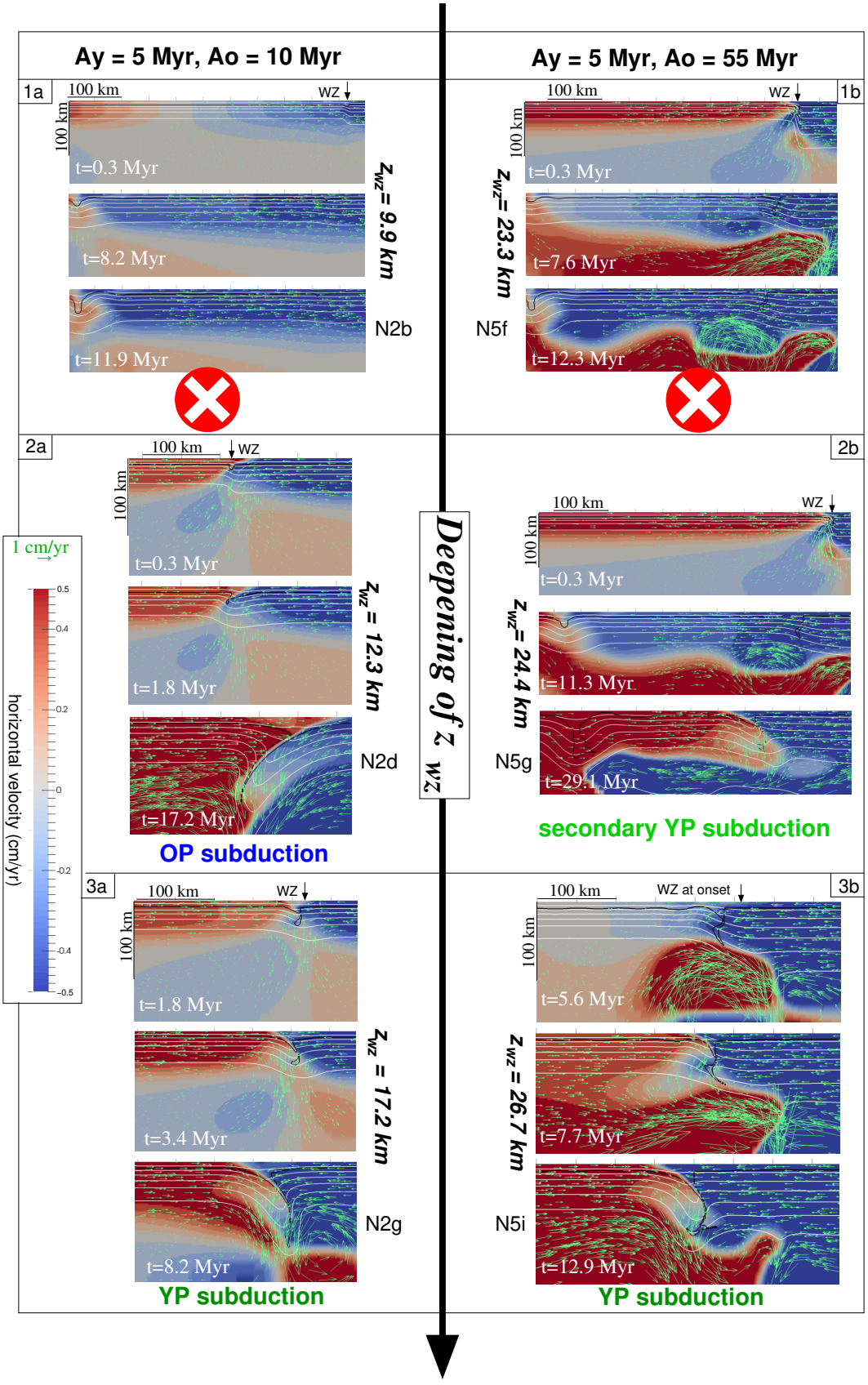

Figure 2: Simulated behaviors for two pairs of plate age (column a: 5 vs 10, simulations N2b, N2d, N2g, b: 5 vs 55, simulations N5f, N5g, N5i): from the failure of convergence localization at the initial fault gouge if the weak zone is not deep enough at the start of convergence (row 1), to initiation of OP subduction or secondary YP subduction (row 2) and initiation of the YP subduction (row 3) as the fault gouge depth at convergence onset is deepened. The thermal transition width is set to 10 km in all cases. Different close-ups on the area of the fault gouge are displayed, the location of which is given by the absolute abscissa of the weak gouge ('WZ') at simulation start (1110 km, Fig. 1), as indicated by the black arrow. The thick black line delimits the crust. One white isotherm every 200°C. Note that the color scale in horizontal velocity is saturated to -0.5 and 0.5 cm/yr. The background color of the table cells is set to grey when the experiment shows an unrealistic evolution of the horizontal force, F_{res} (Table 1).

3.1.2. Subduction of the old lithosphere

The initiation of the subduction of the OP is observed for some plate age pairs, only for moderately shallow fault gouge with respect to the mean depth of the thermal transition, z_{TT} (Fig 1, insert). It occurs quite fast in simulation N2d (5vs10 Myr, TTW =10 km, z_{wz} =12.3 km). Convergence is initially mainly yielding the YP buckling, but soon (1.8 Myr) deformation starts localizing at the weak fault zone (Fig. 2.2a). Convergence is fully accommodated by shearing along the nascent subduction plane from 3.4 Myr, leading to the old plate underthrusting. Subduction initiation is a little longer for simulation N10g (20vs30, TTW =10 km, z_{wz} =26.3 km, Fig. 3.2a), as an initial stage of young plate buckling and of some shortening in the vicinity of the weak fault zone lasts ~7 Myr. The deformation localization becomes efficient at the fault gouge at 8.1 Myr, and is fully transmitted to the incipient subduction plane at 10.3 Myr.

3.1.3. Subduction of the young lithosphere

The initiation of the YP underthrusting is the tectonic behavior the most frequently modeled, obtained for most of the combinations of plate age pair and thermal transition width. The YP subduction can initiate quite fast, such as in simulation N2g (5vs10 Myr, TTW =10 km, z_{wz} =17.2 km). Deformation localization at the fault zone is significant since 1.8 Myr of convergence, then complete at 3.4 Myr when the infant subduction plane is formed, and will remain efficient until the end of the experiment (Fig. 2.3a). The process is moderately longer in simulations N5i (5vs55 Myr, TTW =10 km, z_{wz} =26.7 km) and W7e (10vs30 Myr, TTW =30 km, z_{wz} =22.3 km). A first stage of YP buckling lasts ~5 to 7 Myr before localization at the fault gouge proceeds (Fig. 2.3b and Fig. 3.1b). The embryonic subduction plane accommodates the full convergence rate from 7.7 Myr in simulation N5i to ~10 Myr in simulation W7e. Longer stages of deformation localization at the fault zone are also obtained, such as in Simulation W10f in which it takes ~14.5 Myr (20vs30 Myr, TTW =30 km, z_{wz} =25.0 km, W10f, Fig. 3.2b).

3.1.4. Other modes of convergence accommodation

The preceding three modes of convergence accommodation represent the vast majority of our modeling results (~91% of the simulation total). In a few experiments, convergence is first accommodated during ~17 Myr far away from the fault gouge, by the deformation and shortening of the YP in the vicinity of the left-hand kinematic condition, in a way very similar to a subduction initiation failure. In a second stage, the convergence is partitioned between shortening of the YP close to the kinematic condition and shearing at the weak fault gouge, during the next ~7 to 10 Myr, leading to the formation of an incipient YP underthrusting (N5g, Fig. 2.2b). We refer to this behavior as a secondary localization of convergence at the weak zone entailing YP subduction. Other behaviors are modeled, such as: a secondary and delayed localization of deformation at the transform fault leading to OP subduction (Table S2); simultaneous subduction of both the OP and the YP, either early or delayed; or a subduction initiation during which a subduction polarity reversal occurs.

3.2. Regime Diagram and effects of the fault structure parameters

The results obtained for a narrow transition width (TTW =10 km) are summed up in Fig. 4a, and in Fig. S1 for the wide transition zone (TTW =30 km). For a given plate age pair, we find that the increase in the fault gouge depth z_{wz} yields almost systematically the same tendency: if too shallow, no subduction initiation takes place, whereas for a moderately shallow fault zone, subduction initiates at the fault gouge. Two noticeable exceptions can be stated for TTW = 10 km: 15vs80 Myr for which convergence never localizes at the weak fault, and 20vs55 Myr, for which the range in gouge depth leading to subduction initiation is very limited. The failure of subduction initiation for relatively deep fault gouges is also obtained for TTW = 30 km, but in a much more isolated fashion (Fig. S1). The dozen lithosphere age pairs are classified as a function of the ratio between the age-offset, ΔA, and the YP age, A_y. The parameter $\Delta A/A_y$ allows for gathering quite different pairs of plate age that nonetheless seem to display comparable behaviors. Therefore, the simulation classification based on z_{wz} and $\Delta A/A_y$ shows 3 main domains. The first one corresponds to the absence of subduction initiation and is modeled for all plate age pairs when the fault gouge is shallow in relation to z_{TT}, as aforementioned. Second, the initiation of the OP subduction occurs for a restricted bunch of models, limited both in ranges of plate age pair and of fault gouge depth. Lastly, deep fault gouges at convergence onset generally lead to the underthrusting of the YP at the fault (apart from the two exceptions noticed above). The fault gouge depth at simulation start is hence the major parameter controlling the subduction ability to initiate, but also, when successful, the subduction plane polarity. This z_{wz} effect is observed for all pairs of lithospheric age for TTW = 30 km, and evidenced for 10 plate age pairs (over 12) for TTW =10 km. The thermal transition width TTW only lightly affects the extent of the three main deformation modes (compare Fig. 4a and S1). Its widening to TTW =30 km moderately enlarges the domain of OP subduction initiation in terms of $\Delta A/A_y$, and allows for YP subduction for all plate age pairs and deep z_{wz}. A wide thermal transition thus eases the process of subduction initiation. Moreover, in some very specific cases, the TTW changes the polarity of the incipient subduction zone (10vs30 Myr, when z_{wz} ~25.7 km, Fig 3.2ab), but this does not appear to be a generic effect.

3.3. Tectonic force sustaining convergence at constant rate: Estimate and experiment classification

We compute the horizontal tectonic force, F_{res}, necessary to keep the convergence velocity constant. F_{res} is calculated as the departure from hydrostatic stresses in a reference oceanic column (Christensen, 1992, Supple. Mat): $F_{res} = -\int_0^{z_c} \sigma_{xx} dz + \int_0^{z_c} \rho_{ref}(z) g z dz$, where σ_{xx} is the horizontal normal stress and z_c is the compensation depth (273 km). The F_{res} evolution helps evaluate the subduction sustainability, since in nature compressive horizontal stresses that would be too high could not be supplied, which should stop the local accommodation of convergence and result in a change of the regional kinematic field,

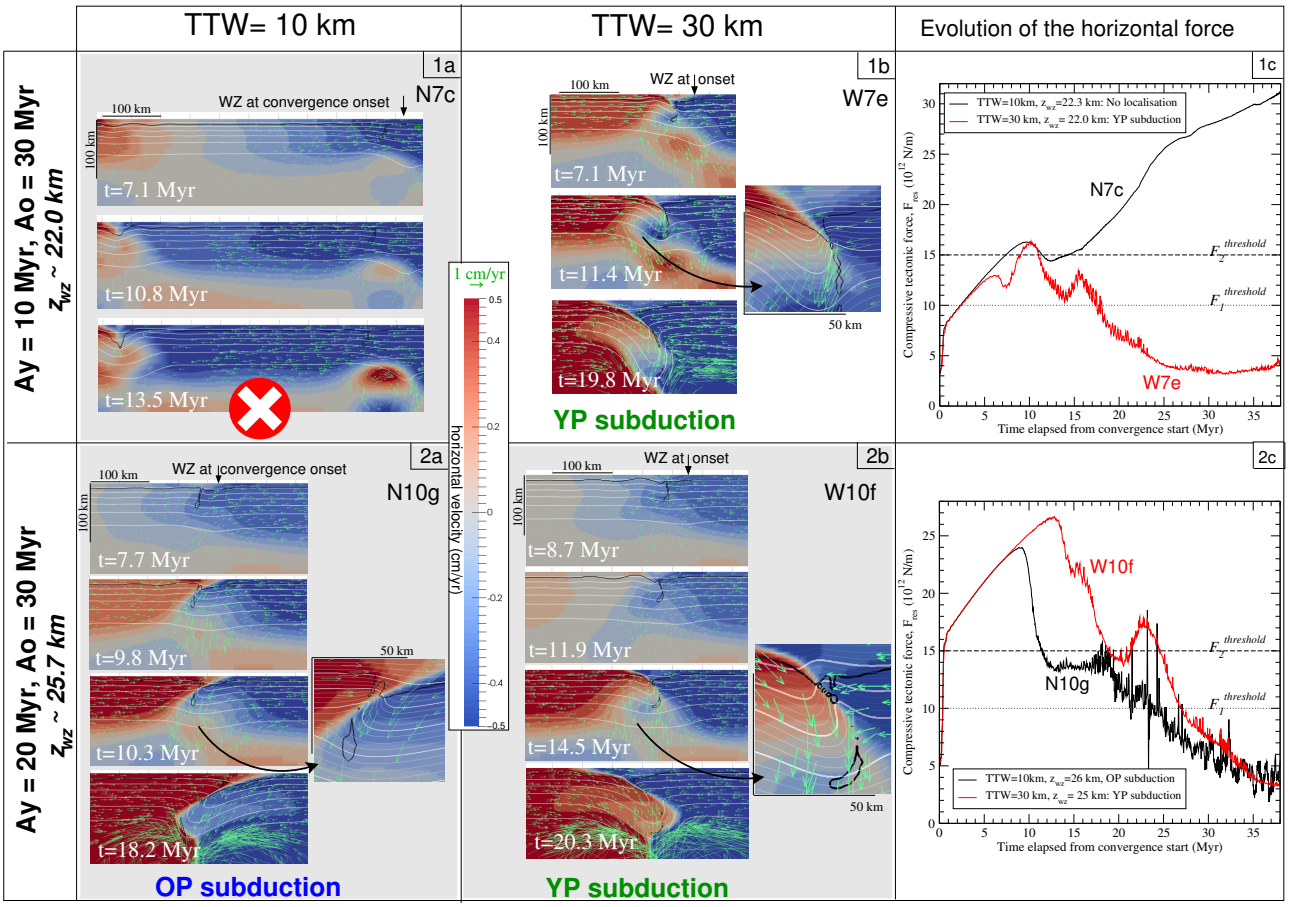

Figure 3: Columns a and b: Simulated behaviors as a function of the thermal transition width (TTW) for two pairs of plate age (row 1: 10 vs 30, 2: 20 vs 30) when the weak zone depth, z_{wz}, is close to 22 and 25.7 km, respectively. See Fig. 2 for the legend. Note that inside the 3 close-ups, the isotherms are depicted very 50^{o}C (thin white lines). Panels 1a and 1b: z_{wz} = 22.3 km (simulation N7c) and 22.0 km (W7e). Panels 2a and 2b: z_{wz} = 26.3 km (N10g) and 25.0 km (W10f). Column c: evolution of the resulting tectonic force for the simulations displayed in columns a (black) and b (red).

or relocate accommodation elsewhere. F_{res} may depend on the convergence rate, set to 1 cm/yr. Mckenzie (1977) and Toth and Gurnis (1998) showed that the convergence must reach a minimum of 1 cm/yr to offset the hindering effect of thermal diffusion. This rate agrees with the convergence length necessary to reach the minimum depth of slab dehydration (~120 km) triggering subduction-related magmatism in approximately 15 Myr, as inferred on average for the Cenozoic subduction zones (Lallemand and Arcay, 2021). Moreover, for the chosen simulation setup, convergente rates $\geq$ 3 cm/yr very frequently yield either the failure of subduction initiation, or flat subduction (Abecassis et al., 2016). We thus prefer to focus on a 1 cm/yr speed.

The question is to choose a limit for this tectonic force to assess an admissible range for F_{res}. Two thresholds are regarded. The maximum horizontal force might come from the net slab pull force, F_{NSP}, arising from a neighboring active subduction zone. F_{NSP} is the fraction of the slab pull (F_b) that is actually available to act on the trailing plate. To account for the F_{NSP} interval assessed in previous studies (Toth and Gurnis, 1998; Conrad and Lithgow-Bertolloni, 2002; Schellart, 2004, see the Supple. Mat. S2), a low threshold $F_1^{threshold}$ = 10^{13} N/m and a high one $F_2^{threshold}$ = 1.5×10^{13} N/m are considerered. This compression threshold range is consistent with the estimated forces initiating a subduction (Zhong and Li, 2019; Li and Gurnis, 2022). The simulated tectonic force is discussed in relation to thresholds $F_1^{threshold}$ and $F_2^{threshold}$ separately.

We detail in the supplementary data (section S2) how we classify the experiments as a function of the F_{res} evolution. In a nutshell, to decide whether the F_{res} evolution is realistic the F_{res} mean during the whole experiment is compared to the chosen threshold. If the latter is exceeded, we consider both the time span and the mean of F_{res} while F_{res} is exceeding the limit (Tables 1 and S2). The simulations are then masked if F_{res} cannot be considered as admissible (Fig. 5). As we explore very different plate age pairs associated with strongly variable lithospheric depths, the fault depth z_{wz} at convergence onset is adimensioned by z_{TT} in the regime diagrams of Fig. 5. We find that if convergence localization does not occur at the fault zone, both compressive thresholds are usually overreached, whatever TTW. When a subduction zone successfully initiates, if TTW =10 km F_{res} generally overreaches $F_1^{threshold}$ as soon as the subducting plate is 10 Myrs old or older. The noticeable exception being OP subduction modeled for 5vs10 Myr. Considering $F_2^{threshold}$ mainly enlarges the domain of simulation acceptability to OP

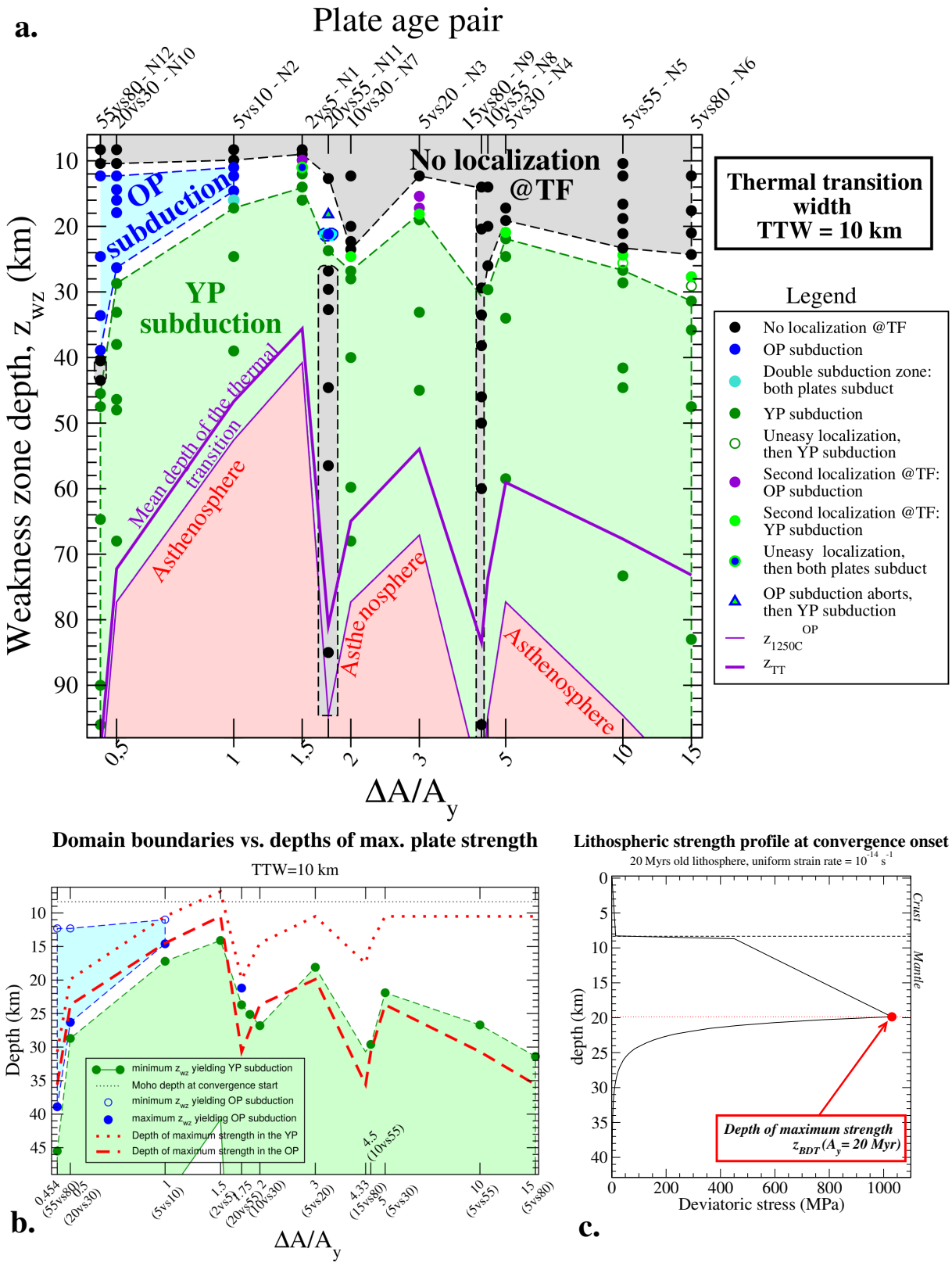

Figure 4: Panel (a): Diagram of convergence regimes for TTW=10 km. Simulation results (circles) are depicted as a function of the plate age pair, represented by the parameter $\Delta A/A_y$, and the depth of the weak fault zone imposed at the start of convergence, z_{wz}. The tags of plate age pairs are defined in Table 1 caption. The domain boundaries (dashed lines) are extrapolated between two plate age pairs. Areas without any experimental point are white. The two purple lines depict, respectively, the depth of the old lithosphere base (1250°C isotherm, thin line), and the reference depth within the thermal transition, z_{TT} (thick line). 'TF': transform fault. Panel (b): Comparison between the limits of the two subduction domains, in terms of initial fault gouge depth, and the depths of maximum strength, z_{BDT} (see panel c) for the two lithospheres. Panel (c): Depth of maximum lithospheric strength, defined by the simulated brittle-ductile transition depth, z_{BDT}. The stress profile is computed for the vertical geotherm of a given lithosphere age, here set to 20 Myr, using the combined rheology described in section 2.1 and the thermo-mechanical constants in Table S1, assuming a uniform strain rate equal to $10^{-14}s^{-1}$.

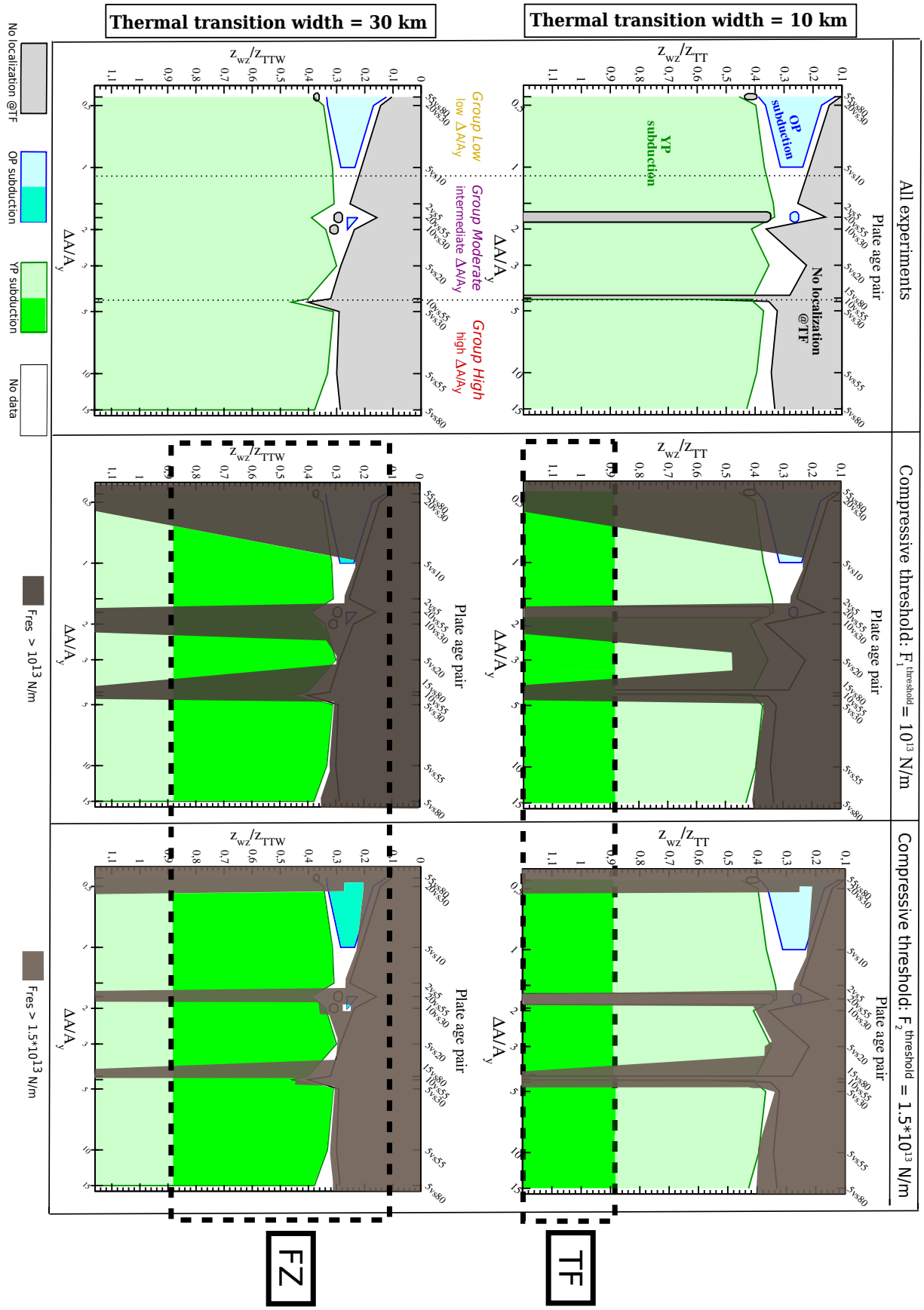

Figure 5: Diagrams of subduction initiation regimes obtained as a function of the thermal transition width, TTW, and the selected threshold in horizontal tectonic force, $F^{threshold}$. Top row: TTW =10 km; bottom row: TTW =30 km. Left column: no threshold in the compressive force. Middle and right columns: the compressive threshold is set to $F_1^{threshold}$ = 10^{13} N/m and $F_2^{threshold}$ = 1.5×10^{13} N/m, respectively. The ordinate axis represents the weak fault gouge depth at convergence onset, z_{wz}, adimensioned by the reference depth of the thermal transition, z_{TT}. To make graphs easier to read, the simulation points are not displayed. The dashed rectangles 'TF' and 'FZ' delimit the parameter ranges assumed for oceanic transform faults and fracture zones, respectively.

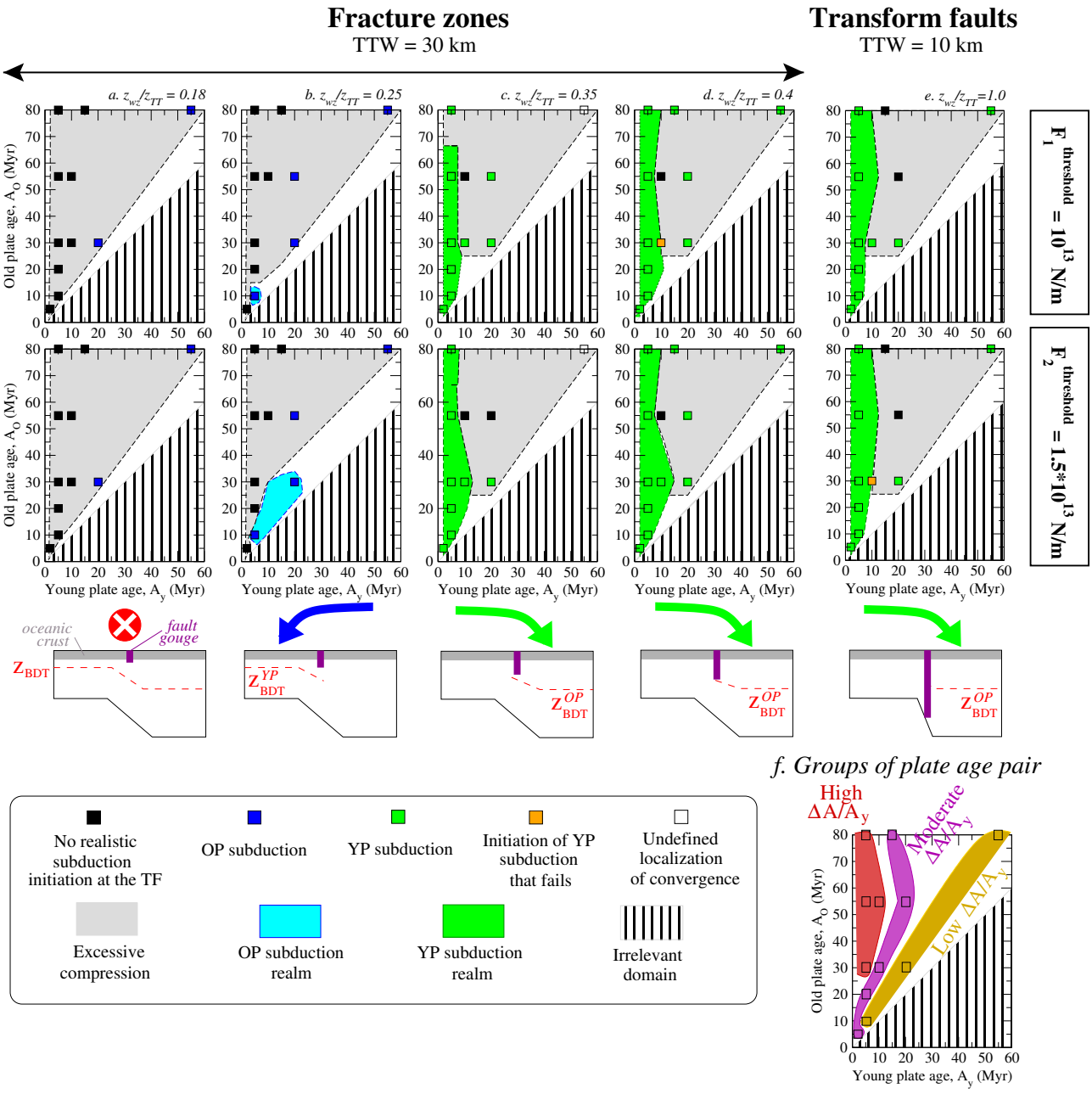

Figure 6: (a) to (e): Diagrams of convergence accommodation regimes as a function of the two plate ages A_y and A_o, by considering both the obtained deformation style and the evolution of the horizontal tectonic force. Different thermal transition widths, TTW and ratios of the weak fault gouge depth to the thermal transition reference depth z_{wz}/z_{TT} are selected to represent fracture zone settings on one hand (panels a-d), and transform fault configurations on the other hand (panel e, see section 3.4). The threshold defining admissible compressive stresses is set to either $F_1^{threshold} = 10^{13}$N/m (top row) or $F_2^{threshold} = 1.5\times10^{13}$N/m (bottom row). The dashed areas depict the domains where the young lithosphere age would exceed the old lithosphere one. The sketches below illustrate the relationship between the modeled structure setup and the simulated polarity of the subduction zone, if any. 'z_{BDT}' represents the depth of the brittle-transition depth, the exponent 'YP' or 'OP' refers to the considered plate. (f) Representation in a $A_y - A_o$ graph of all investigated plate age pairs, showing their respective belonging to the three groups defined in section 4.1.

subduction simulated with the plate pair 20vs30 Myr. The wide thermal transition TTW =30 km does not globally modify the bounds of the realistic realm previously described. We still notice that by considering $F_2^{threshold}$, F_{res} becomes admissible for OP subduction obtained for 10vs30 Myr as well as for YP subduction for 10vs30 and 10vs55 Myr. The widening of the thermal transition eases the process of subduction initiation, in agreement with the conclusions of section 3.2. Choosing a significantly higher limit for the available tectonic force, such as 5×10^{13} N/m (Wu et al., 2008) would imply that all our experiments could be deemed as realistic (as displayed in the left column of Fig. 5). Indeed the maximum average tectonic force simulated when subduction initiates is found in simulation W12h (55vs80 Myr), and equals 4.02×10^{13} N/m (Table 1, see also Table S2).

3.4. *Transform fault vs fracture zone setups*

The system of simulation plotting in Fig. 4a and S1 makes the comparison to geological records of subduction initiation

difficult. A convenient displaying way is to plot the results as a function of the two lithospheric ages at convergence start, A_o and A_y. This necessitates to choose an identical fault gouge depth for all plate age pairs, while the range in z_{wz} is highly variable. We thus adimension z_{wz} by the reference depth z_{TT}. As discussed in section 2.2, an active transform fault is assumed to present a narrow thermal transition and a deep weak fault gouge (TTW =10 km and $z_{wz} \sim z_{TT}$), which leads to $z_{wz}/z_{TT} \sim 1$. In contrast, a wide thermal transition and a shallow weak fault zone are expected for an inactive fracture zone (TTW =30 km and $z_{wz} < z_{TT}$). In Fig. 6 an aged fracture zone may present a very low z_{wz}/z_{TT} ratio, here set to 0.18, whereas a fault having recently become inactive may have a higher one, set to 0.4. Note that the boundaries of subduction initiation regimes are drawn by restricting the subduction realms to simulations showing admissible tectonic forces.

Subduction initiation with realistic compressive stresses is impeded for too shallow fault gouges such as $z_{wz}/z_{TT} = 0.18$ (Fig. 6, column a). The initiation of OP subduction is best favored for ratios z_{wz}/z_{TT} close to 0.25, and for low offsets in plate ages. Considering a high compressible threshold enlarges the regime of OP subduction (Fig. 6, column b). When $z_{wz}/z_{TT} \geq 0.35$, subduction initiation is achieved via YP underthrusting only, whatever the plate age offset, but the domain of realistic compression is not significantly affected by the fault depths or the compressive threshold (Fig. 6c, d, e). Finally, no OP subduction initiates at a transform fault undergoing compression in our modeling. OP subduction is simulated only for fracture zone setups for which the strike-slip motion would have stopped a long time ago (with respect to the considered plate ages). In contrast, the setup mimicking an active transform fault allows for YP underthrusting only.

4. Analysis

4.1. Influence of the respective 'deformabilities' of each lithosphere

The changes from a mode of convergence accommodation to another depend on the considered plate pair. Three groups are defined by taking into account the whole pattern of tectonic behaviors that a plate age pair can display (Fig. 5). In the first group, the three deformation modes occur as a function of the fault gouge depth at convergence onset, z_{wz}. This group corresponds to low $\Delta A/A_y$ ($\leq$1, 'Group Low'). In the second end-member group, subduction initiation either fails, or corresponds to the YP underthrusting, depending on z_{wz}. This group is defined by high $\Delta A/A_y$ ($\geq$4.5, 'Group High'). In the in-between group, the initiation mode is more disparate, and is more sensitive to set-up conditions: either YP subduction is simulated for a very narrow range of z_{wz} (20vs55 Myr) or only if TTW =30 km (15vs80 Myr), or polarity depends on TTW (10vs30 Myr), or OP underthrusting is always postponed (2vs5 Myr), or OP subduction is both delayed and restricted to a narrow TTW (5vs20 Myr). This last group corresponds to intermediate $\Delta A/A_y$ (1< $\Delta A/A_y$ <4.5, 'Group Moderate').

The relationship between the tectonic behavior pattern and $\Delta A/A_y$ is interpreted as reflecting the dominating effect of the relative plate deformabilities. In Group High, the thin plate first undergoes both a significant buckling and shearing, while the OP is moderately deformed (Fig. 2, column b). The relatively high YP ability to deform focuses the convergence accommodation within the YP and favors YP subduction. Moreover, because of its softness, the YP bends at a steep dip angle and the incipient subducting slab is almost sub-vertical. This could explain why the weak fault gouge is already more or less the embryonic subduction plane. In Group Low, the plate strength contrast is moderately low, both plates have roughly similar capacities to subduct and the subduction zone polarity is selected as a function of the fault gouge depth. Group Moderate constitutes a midway pattern: the mode of convergence accommodation is more sensitive to the whole structural setup, notably to the TTW. The hindering effect of a narrow thermal transition on subduction initiation (20vs55 and 15vs80) is discussed in Section S4.

Finally, if $A_o \gtrsim$30 Ma, the tectonic pattern that a plate pair can display is essentially a function of the age constrast: the larger the age offset, the higher the prevalence in 'YP subduction only'-pattern (Fig. 6f). In contrast, when the OP is younger than 30 Myr, the plate pair behavior is also dependent on the YP age.

4.2. Conditions for YP subduction: Comparison between z_{wz} and the depth of maximum strength within the OP

We compute for all investigated lithospheric ages, the simulated strength profile (section 2.1), assuming a constant strain rate of 10^{-14}s^{-1}. The lithospheric stress is maximum at the depth where the major deformation mode changes from brittle to viscous, and is labeled the brittle-ductile depth (Figs. 4c and S2). This brittle-ductile transition at simulation start roughly corresponds to the ~600^{o}C isotherm (Fig. S2). The brittle-ductile transition depth predicted for each of the two plates surrounding the fault zone is compared to the minimum depth of the fault gouge leading to YP subduction initiation, $z^{YPS}_{wz\ min}$. This minimum $z^{YPS}_{wz\ min}$, is strongly correlated to the brittle-ductile transition depth of the OP when TTW =10 km (Fig 4b). The correlation becomes very good for TTW =30 km for all plate age pairs (Fig. S3). In contrast, $z^{YPS}_{wz\ min}$ does not correlated to the brittle-ductile transition depth of the YP when $\Delta A/A_y \geq 5$. We conclude that, in our modeling, the brittle-ductile transition depth of the OP at convergence initiation is a satisfying proxy for the shallowest depth of the fault gouge triggering YP subduction.

4.3. Heat dissipation at the brittle-ductile transition promotes the formation of the subduction plane, and affects F_{res}

To test the previous conclusion, let us compare the evolutions of the tectonic force, F_{res}, and of the thermal and compositional structures of the incipient subduction zone, based on Simulation W10f (20vs30, TTW =30 km, z_{wz} =25 km, Fig. 3.2b,c). Compressive stresses are first increasing until ~13 Myr, before a fast and strong decrease. This time matches the end of convergence localization along the incipient subduction plane (~14.5 Myr, Fig. 3.2b). One may notice that, at 14.5

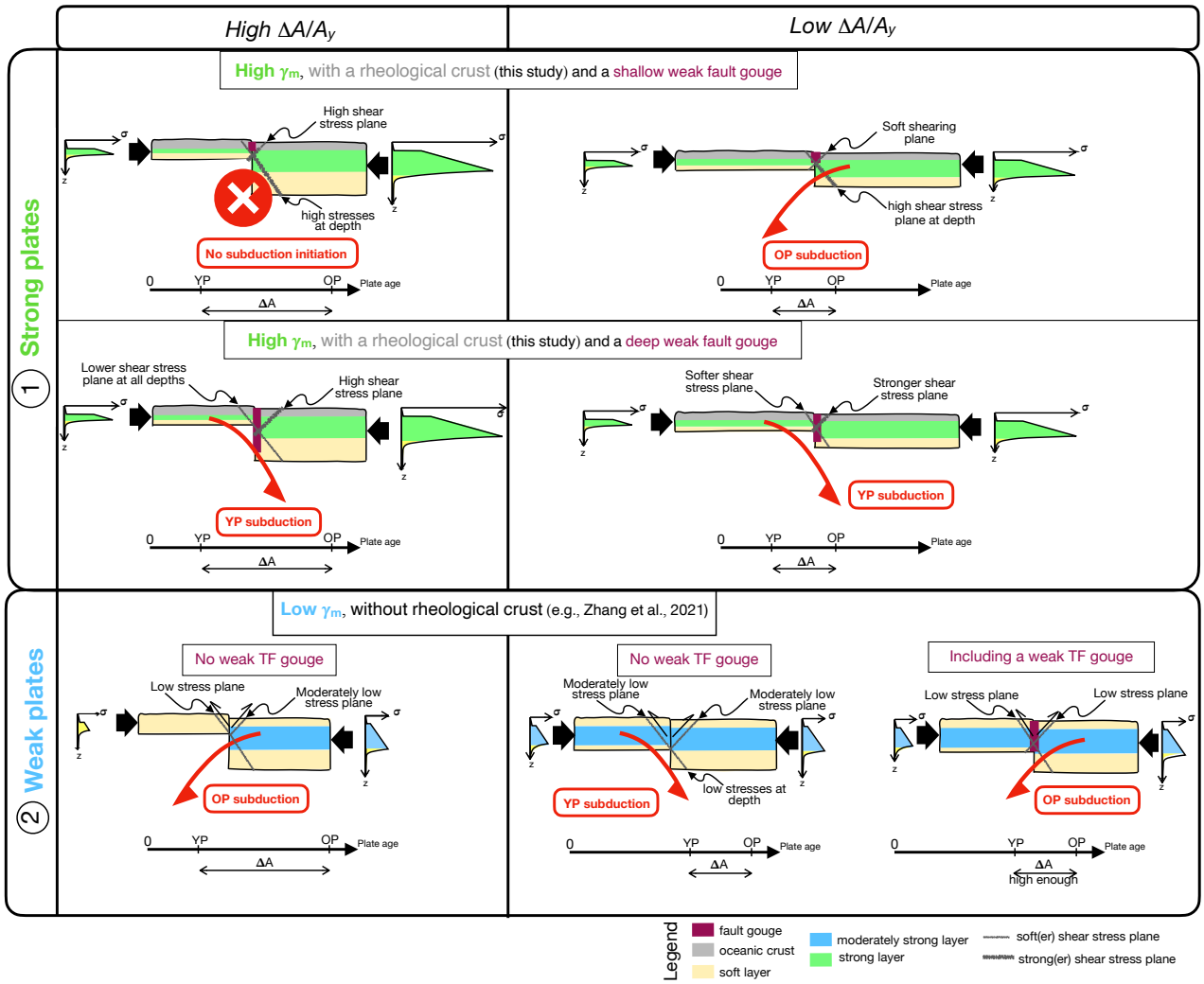

Figure 7: Sketches illustrating the simulated process of subduction initiation. The figure compares two geodynamic situations: the one modeled in this study (row 1) in which the lithospheric strength is high, to a model setup where the lithospheric strength is much weaker (row 2), as modeled for instance by Zhang et al. (2021) (see section 4.4 for more details). Two end-member cases for the parameter $\Delta A/A_y$ are considered, a low one (left-hand side column) and a high value (right column). Row 1 is subdivided into two parts, depending on the depth of the transform fault gouge at convergence onset, either shallow (first line) or relatively deep (second line). In row 2 considering weak plates, the transform fault gouge is either included or not. The lithospheric layers are color-coded as a function of their relative strength, the amplitude of which is depicted by the schematic 'Christmas' tree (still at scale) located at the plate extremity. The layers made of oceanic crust in grey and in purple are very weak layers.

Myr, the 600^{o}C isotherm of the OP is rising in the vicinity of the bottom of the weak gouge, up to ~28 km depth, without any associated upward flow. This depth fits with the expected brittle-ductile transition depth for a lithospheric age of ~46 Myr (Fig. S2), which is close to the OP age at this time. A maximum in the heat dissipation rate, caused by shear heating, is occurring at the mantle brittle-ductile transition depth (5.1×10^{-5}W.m^{-3}, yielding a temperature rise to 650^{o}C) and explains the 600^{o}C isotherm uplift, which in turn results in a localized mantle softening. The lowering in F_{res} at the same time means that once the nascent subduction plane has reached the brittle-ductile transition depth within the OP, not only the convergence localization is almost completed, but also most of the required work is done. Similar parallel evolutions are observed for Simulation W7e: the F_{res} initial rising is followed by a fast decrease that occurs when the thermo-mechanical development of the main shear plane extends up to the brittle-ductile transition depth of the OP (Fig. 3.1b,c).

Our interpretation is twofold. Horizontal compressive stresses do not peak when the whole proto-overriding plate has been cross-cut by the incipient subduction plane, but instead when the latter has reached a rather shallow depth (between 20 and 35 km depth), i.e. the brittle-ductile transition depth of the upper plate. Heat dissipation at this depth acts as a softening agent that helps the further F_{res} drop on one hand, but also the continuation of the weak zone deepening and shear plane development. The brittle-ductile transition depth of the OP is thus deemed as controlling the stress peak that has to be overcome for initiating a YP subduction, in agreement with the conclusion derived in the preceding section. We observe the same concomitant evolutions for F_{res}, shear heating, and subduction plane development in the case of OP underthrusting, the depth of maximum resistance that has to be achieved being then the brittle-ductile transition within the YP (section S3). We observe that, whatever the subduction zone polarity, the shear stress

along the incipient subduction plane globally varies between 28.7±3.3 MPa at 12.5 km depth and 48±3 MPa at 20 km depth after ~12 Ma.
Eventually, our results confirm that an initially vertical weak zone is not promoting the initiation of a subduction zone, and that an adequately-dipping shear plane has to form first (e.g., Doin and Henry, 2001; Boutelier and Beckett, 2018; Hamai et al., 2018).

4.4. How do deformation localization and the selection of the underthrusting direction proceed?

Let us recall that the fate of a subduction initiation can be predicted by comparing z_{wz} at convergence onset to the brittle-ductile transition depth in the future upper plate (Section 4.2). A subduction zone initiates if a weak down-dipping shear plane develops. This occurs in our simulations if the latter can reach the depth of maximum strength in the overriding lithosphere, to cut off the high resistance near the brittle-ductile transition.
Regarding the nascent subduction zone polarity, if the low shear stress plane is close to the depth of the brittle-ductile transition of the OP, then YP subduction initiates (Fig. 4c, S3). Nevertheless, the OP is still the denser lithosphere. One might expect that a deep weak gouge combined to a large density offset would then trigger OP subduction. We observe the opposite (Fig. 7-1, high $\Delta A/A_y$, Group High). The horizontal density gradient across the fault gouge is not governing the incipient underthrusting polarity. The way convergence is accommodated is rather mainly a function of the plate strength contrast (Section 4.1). We posit that, at large $\Delta A/A_y$, the nascent subduction polarity is defined, on one hand, by the higher plate capacity to deform, and on the other hand, by the possibility through the initial fault gouge extent, to somehow cancel (or at least decrease) the future upper plate resistance to shearing. The systematic YP subduction modeled for large $\Delta A/A_y$ agrees with other numerical experiments modeling stiff lithospheres, when the brittle yield strength increase for the mantle γ_m, > 0.8 (Zhang et al., 2021). In our study, we choose γ_m = 1.6 (Table S1). At low $\Delta A/A_y$ (Group Low), the polarity change for shallowing z_{wz} results from the fact that, for a too shallow z_{wz}, shearing the thick OP to form a subduction plane is too expensive, while shearing the YP is more efficient. The latter option 'only' requires to reach the shallower brittle-ductile transition in the YP, even if it also implies to make the OP bend with a high energetic cost. Furthermore, as the two plate deformabilities are closer, the effect of the density difference might be enhanced.
The situation is different for weak plates. Zhang et al. (2021) show that without any weak fault gouge, if the lithospheres on both sides of the thermal stair-step are soft (γ_m =0.3), OP subduction initiates when ΔA ≥30 Myr, with a minor influence of the YP age (Fig. 7-2, left). Alternatively, YP subduction occurs, unless a weak fault gouge is included between the lithospheres (Fig. 7-2, right). Zhou and Wada (2022) and Arcay et al. (2020) obtain consistent modeling results for a low mantle plastic strength ($\gamma_m \leq 0.3$) and a very weak vertical interplate domain, that systematically lead to OP subduction (except if the weak gouge is narrowed for Zhou and Wada, 2022). Hence for soft lithospheres, the lateral density gradient may have a stronger influence than the resulting 'small' plate strength contrast in selecting the subduction polarity, as also observed by Boutelier and Beckett (2018).

5. Discussion

5.1. Model setup considerations

The brittle-ductile transition simulated for the mantle corresponds to the ~600^{o}C isotherm, consistent with the temperature inferred for deep earthquakes at oceanic transform faults (Engeln et al., 1986; Abercrombie and Ekström, 2001; McKenzie et al., 2005). Our rheological model is thus a simple but reasonable proxy. However, the subducting plate age can hardly exceed 10 to 30 Myr in our modeling, otherwise compressive stresses become non-viable (section 3.3), suggesting that our lithospheric rheology is somewhat too stiff. Extra experiments performed with slightly softer plates show that our main results are not modified. A lower mantle yield stress-increase with depth, γ_m, would deepen the brittle-ductile transition, in agreement with temperatures at the brittle-ductile transition > 700-900^{o}C at oceanic transform faults (Kohli and Warren, 2020; Kohli et al., 2021) and deep seismicity (McGuire et al., 2012; Roland et al., 2012; Wolfson-Schwehr et al., 2014; Yu et al., 2021). This would imply to deepen the minimum z_{wz} to get subduction initiation, but we are rather confident that our main conclusions would remain unchanged: YP subduction is likely to remain predominant as long as γ_m >0.8 (Zhang et al., 2021, see 4.4). We consider that decreasing γ_m much below 0.8 is not reasonable, as discussed in Arcay et al. (2020). Nevertheless, it could be strongly lessened for a mature subduction zone, if a significant part of the convergence is seismically accommodated within the lithospheric mantle (Karato and Barbot, 2018).
Simulating a much weaker oceanic crust can affect the boundaries between the different subduction regimes ((Section S6 , Table S3) and destabilize the initiation process. Still, the general pattern of the subduction regimes shown in Fig. 4 remains similar.
Our modeling approach neglects elasticity, but elastic deformation has been shown to not drastically affect the mode of subduction initiation simulated in visco-plastic (brittle) models (Thielmann and Kaus, 2012; Zhou and Wada, 2022; Li and Gurnis, 2022). Our 2D-modeling setup is certainly more appropriate to study a fracture zone undergoing compression where active strike-slip is absent. Neglecting the 3D effects of the strike-slip motion during early compression at a transform fault could make subduction initiation more difficult, since the strike-slip-related strain rate might soften the fault gouge (Zhou and Wada, 2022), as shown by Zhong and Li (2023). Moreover, our model setup does not account for some sources of compositional heterogeneities favoring weakening and likely to promote subduction initiation, such as continental or arc relics, or the proximity of a mantle plume and/or of an active spreading center (Lallemand and Arcay, 2021). Finally, the importance of the YP subduction initiation predicted in our study agrees with the geological records (Lallemand and Arcay, 2021, and see below).

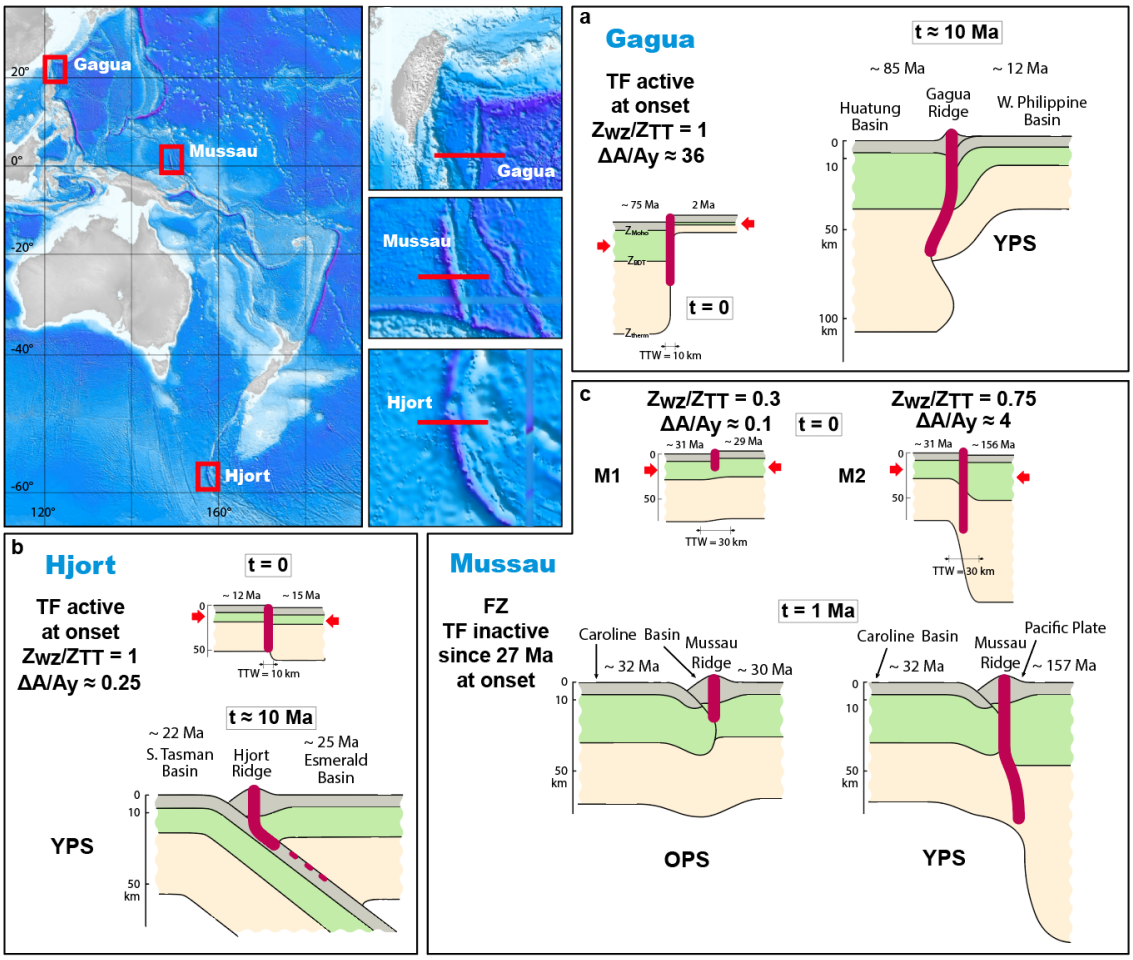

Figure 8: Proposed scenarios of subduction initiation at (a) Gagua ridge, (b) Hjort and (c) Mussau trenches. In each panel, the tectonic setting is sketched at the convergence onset ('t=0)' then at the final stage of convergence, corresponding to either the subduction stop (Gagua) or the present-day state (Hjort, Mussau). The color-coding of the different lithospheric layers refers to the one used in Fig. 7. 'YPS' and 'OPS' mean YP subduction and OP subduction, respectively.

5.2. *Comparison to geological records of subduction initiation at transform faults and fracture zones*

A detailed examination of natural cases of subduction zone initiation along a transform fault or fracture zone in the Cenozoic (Lallemand and Arcay, 2021) has led us to exclude many of them like Izu-Bonin-Mariana, Puysegur or even Romanche because of compositional heterogeneities (relic arcs or continental strips) adjacent to the nascent subduction zone. We suspect that these heterogeneities conditioned the polarity of the initial underthrusting (e.g., Leng and Gurnis, 2015). We will therefore focus on two recent cases of oceanic transform faults and one fracture zone undergoing/having undergone significant shortening : Gagua Ridge, Hjort, and Mussau (Fig. 8), even if minor heterogeneities might exist.

Regarding the Gagua Ridge (Fig. 8a), it has been proposed either a single or a double phase of initiation of subduction of the Eocene West Philippine Basin beneath the Early Cretaceous Huatung Basin at ~50 Ma (Deschamps et al., 2000) and at ~24 Ma (Eakin et al., 2015), none of them leading to a mature subduction zone. We focus here on the first one, since the second one has probably reactivated the former deformation zone. Recent sampling at the top of the ridge not only confirms the Early Cretaceous age but also attests for arc volcanism of the same age (Zhang et al., 2022). Incidentally, this recent discovery also introduces the notion of compositional heterogeneity mentioned above. At onset, the combination of a high $\Delta A/A_y$, a narrow thermal transition and z_{wz}/z_{TT} =1 because the transform fault was active satisfied the conditions for incipient subduction of the YP as shown in Fig. 9c.

The age contrast ΔA in the case of Hjort Trench (Fig. 8b) belonging to the transpressional Macquarie Ridge complex is much smaller, e.g. a few Myrs. Time of subduction initiation onset was estimated 6 to 11 Myrs ago (Meckel et al., 2003, 2005). The age of the South Tasman Basin (neo-subducting plate) varied laterally between 16 Ma in the north and 9 Ma in the south at the time of onset, whereas those of the Esmerald Basin ranged between 14 Ma and 19 Ma respectively. On one side, the plot of the mean ages of the lithospheres on either side of the transform fault falls in the vicinity of the YP subduction regime without belonging to it. On the other side, the activity of the transform fault at the time of onset (TTW =10 km, z_{wz}/z_{TT} =1) precludes the eventuality of OP subduction in our simulations (Fig. 9c).

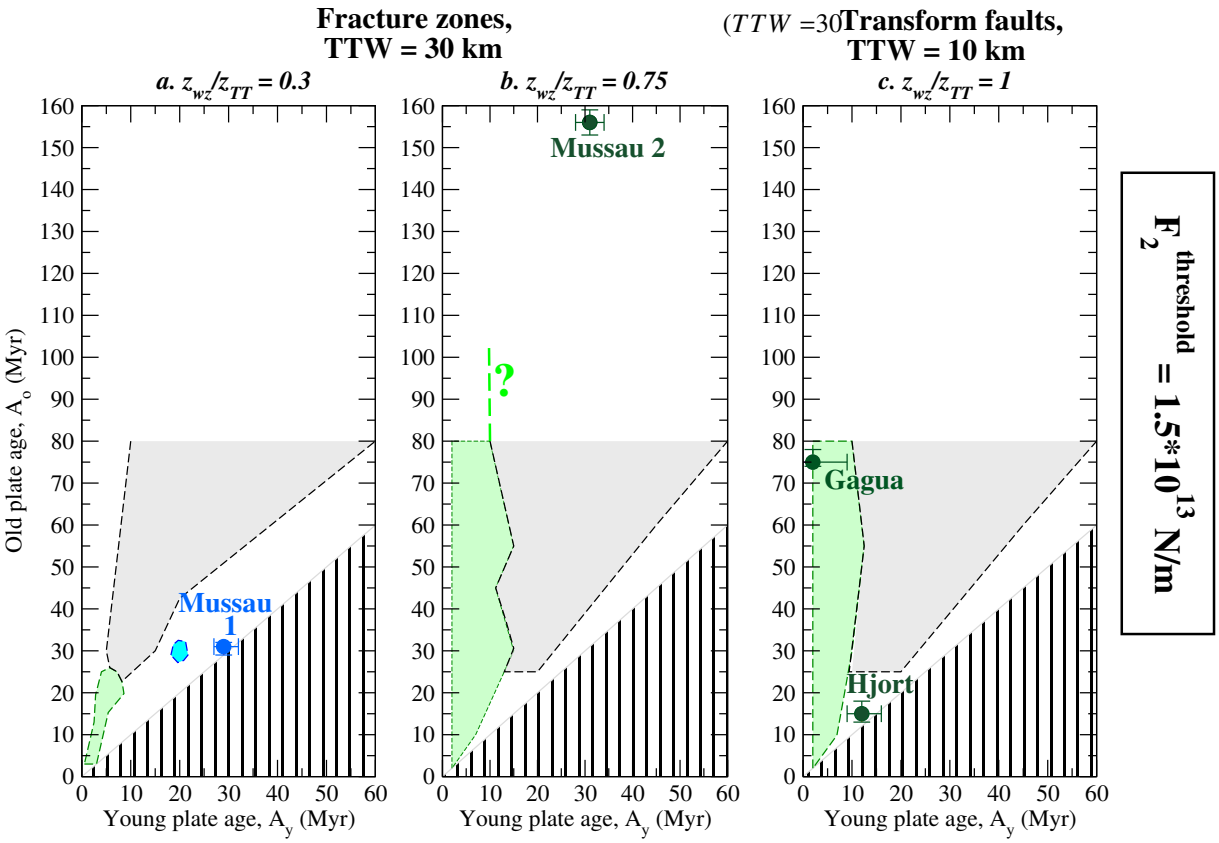

Figure 9: Modes of convergence accommodation depicted as a function of the two lithosphere ages at convergence onset, A_y (x-axis) and A_o (y-axis), for 3 different ratios z_{wz}/z_{TT} related to: a fracture zone (a, b), and a still active transform fault (c). The TTW is set to 30 km in (a) and (b), and to 10 km in panel (c). The boundaries of the different regimes in panels a and b not displayed in Fig. 6 are defined using experimental results in the supplementary Figure S4. They are extrapolated in panel b to the lithospheric ages observed in the geological records. The threshold in the simulated compressive force is set to $F_2^{threshold} = 1.5 \times 10^{13}$ N/m. The scenarios proposed for Mussau 1 and 2 differ by the assumed lithosphere nature on the Eastern side of the fracture zone: either the Caroline Basin (a) or the Pacific plate (b, see section 5.2). The legend refers to the one used in Fig. 6.

The case of the Mussau Trench is less constrained than the two previous ones because it has never been re-explored since the pioneer survey onboard R/V Vema in the late 70's (Weissel and Anderson, 1978). The mean age of the Oligocene Caroline Basin along the trench is ~32 Ma. There is still a debate regarding those of the neo-upper plate which could be either the same basin with a slightly younger crust (Hegarty et al., 1983, ~30 Ma, scenario Mussau 1 in Fig. 8c & 9a), or the upper Jurassic Pacific Ocean crust (Weissel and Anderson, 1978; Gaina and Müller, 2007, scenario Mussau 2 in Fig. 8c & 9b). It has been proposed by Hegarty et al. (1983) that the convergence started only 1 Myr ago, which, a priori, seems very little considering the low convergence rate and the flexural profile of the Caroline Basin under/against the Mussau Ridge. We observe that the Mussau 1 scenario (TTW =30 km, low $\Delta A/A_y$ and z_{wz}/z_{TT} ~0.3) is close to the viable domain of OP subduction, while the Mussau 2 scenario of YP subduction km, moderate to high $\Delta A/A_y$ and z_{wz}/z_{TT} ≈0.75), even if it falls outside of our simulation set, is likely to fail (Fig. 9c and 9a,b).

5.3. *A paradoxical situation: Conditions promoting subduction initiation in a cold Earth vs. conditions of self-sustained subduction*

Hall and Gurnis (2003) and Gurnis et al. (2004) investigated the conditions to get the thick plate subduction, arguing that the negative buoyancy of the incipient subducting slab must be high enough to reach self-sustainment. However, numerous subduction zones having become self-sustained initiated by the underthrusting of a young to very young lithospheres (<30 Myr, Lallemand and Arcay, 2021). Our thermo-mechanical study leads up to consistent results, showing that subduction initiation is often easier for young, and still buoyant, incoming plates. We further observe that, once the incipient subduction plane has reached the brittle-ductile transition within the proto-overlapping plate, compressive stresses keep on decreasing on average up to the simulation end (~35-45 Ma) to a low final tectonic force (3 to 5×10^{12}N/m, Fig. 3.2c and S6, section S5). One noteworthy secondary compression rise occurs when the downgoing slab enters the asthenosphere where, consequently, it has to activate flows throughout the underneath mantle layer. Once this is done, a last compression decrease occurs, related to the slab pull development (e.g., Hassani et al., 1997) still without achieving subduction self-sustainment.

Consequently, the subduction conditions must evolve between the initiation and mature stages. For instance, in the geological records (Lallemand and Arcay, 2021) as well as in our simulations, the incipient slab development usually requires ~15 Myr

to reach a ~120 km depth, which ages the subducting plate by the same amount. Moreover, once started the subduction process is possibly partly self-lubricating, thanks to the weakening effect of dehydration-related fluids (e.g., Peacock and Hyndman, 1999). An alternative or additional factor helping to reach the mature stage could rely on the subducting crust eclogitization (Doin and Henry, 2001).

6. Conclusions

We performed thermomechanical experiments to investigate how a subduction zone may initiate at an oceanic transform fault or fracture zone when compression is imposed. Our results show the major effect of the initial fault structure, especially of the fault gouge depth, in the absence of any preexisting structural heterogeneity. Subduction initiation is successful if the gouge depth is close to the depth of the brittle-ductile transition in the future overriding plate. Old plate subduction initiates if z_{wz} equals ~25 to 35% of the mean of the 2 plate thicknesses (z_{TT}) and if the age offset scaled by the younger age is moderate (i.e. $\Delta A/A_y \leq 3$). Young plate subduction is modeled when z_{wz} is $\gtrsim$40% of z_{TT}, whatever the age offset. A narrow thermal transition between converging plates is a somewhat hindering factor to localize deformation, possibly because the initial gouge may be misplaced with respect to the vertical oscillations of the Moho associated with plate buckling prior to the subduction plane formation. Instead, the propitious effect observed for TTW =30 km could come from the widening of the space available for plate buckling. Since deep gouges promote YP underthrusting in our modeling, only YP subduction is predicted at active transform faults characterized by deep faults, whereas OP subduction is restricted to some old fracture zones where shallower gouges are expected. The significant predominance of YP subduction results from the strong influence of the plate strength contrast when lithospheres are stiff: subduction initiation depends on the possibility to form a low shear stress plane across the future upper plate. Our modeling results are consistent with the recent records of subduction initiation at former transform faults or fracture zones in the Western Pacific. YP subduction is predicted at Gagua Ridge and Hjort trench, as observed, as well as at Mussau trench if the lithosphere age is Jurassic on the eastern side of the ridge.

Acknowledgements

This study has been supported by CNRS-INSU (National Institute of Universe Science) program 'TelluS-SYSTER'. We thank Stéphane Arnal and Fabrice Grosbeau for the maintenance and development of the lab cluster of computing nodes on which all numerical experiments were performed. We warmly thank Mrs. Farida Benmouffok for her coaching help. Zhong-Hai Li and an anonymous reviewer are acknowledged for their thoughtful reading and their very constructive comments that improved the paper, as well as R. Bendick for having handled the manuscript.

Competing interests

The authors declare no competing interests.

References

Abecassis, S., Arcay, D., Lallemand, S., 2015. How to model an incipient subduction across a transform fault?, in: abstracts of the 14th International Workshop on Modeling of Mantle and Lithosphere Dynamics, Aug. 31-Sept. 5, Oérons, France. URL: http://geoweb.cse.ucdavis.edu/cig/events/calendar/2015-14th-intl-mantle-and-lithospheric-dynamics/.

Abecassis, S., Arcay, D., Lallemand, S., 2016. Subduction initiation at fracture zones : conditions and various modes, in: abstracts of the GeoMod conference, Oct. 17-20, La Grande Motte, France. p. 14. URL: http://geomod2016.gm.univ-montp2.fr/Home.html.

Abercrombie, R.E., Ekström, G., 2001. Earthquake slip on oceanic transform faults. Nature 410, 74–77.

Arcay, D., 2017. Modelling the interplate domain in thermo-mechanical simulations of subduction: Critical effects of resolution and rheology, and consequences on wet mantle melting. Phys. Earth Planet. Inter. 269, 112–132. URL: https://doi.org/10.1016/j.pepi.2017.05.008, doi:10.1016/j.pepi.2017.05.008. doi:10.1016/j.pepi.2017.05.008.

Arcay, D., Lallemand, S., Abecassis, S., Garel, F., 2020. Can subduction initiation at a transform fault be spontaneous? Solid Earth 11, 37–62. doi:https://doi.org/10.5194/se-11-37-2020.

Baes, M., Sobolev, S.V., Quinteros, J., 2018. Subduction initiation in mid-ocean induced by mantle suction flow. Geophys. J. Int. 215, 1515–1522. doi:10.1093/gji/ggy335.

Behn, M., Boettcher, M., Hirth, G., 2007. Thermal structure of oceanic transform faults. Geology 4, 307–310. doi:10.1130/G23112A.1. 10.1130/G23112A.1.

Boutelier, D., Beckett, D., 2018. Initiation of subduction along oceanic transform faults: Insights from three-dimensional analog modeling experiments. Frontiers in Earth Science 6, 204. URL: https://www.frontiersin.org/article/10.3389/feart.2018.00204, doi:10.3389/feart.2018.00204.

Chopra, P., Paterson, M., 1981. The experimental deformation of dunite. Tectonophysics 78, 453–473. doi:10.1016/0040-1951(81)90024-X.

Christensen, U.R., 1992. An Eulerian technique for thermomechanical modeling. J. Geophys. Res. 97, 2015–2036.

Conrad, C., Lithgow-Bertolloni, C., 2002. How mantle slabs drive plate tectonics. Science 298, 207–209.

Deschamps, A., Monié, P., Lallemand, S., Hsu, S.K., Yeh, J., 2000. Evidence for early cretaceous oceanic crust trapped in the philippine sea plate. Earth Planet. Sci. Lett. 179, 503–516.

Detrick Jr, R.S., Purdy, G., 1980. The crustal structure of the Kane fracture zone from seismic refraction studies. J. Geophys. Res. 85, 3759–3777.

Doin, M.P., Henry, P., 2001. Subduction initiation and continental crust recycling: the roles of rheology and eclogitization. Tectonophysics 342, 163–191.

Eakin, D., McIntosh, K., Van Avendonk, H., Lavier, L., 2015. New geophysical constraints on a failed subduction initiation: The structure and potential evolution of the gagua ridge and huatung basin. Geochem. Geophys. Geosyst. 16, 1–21.

Engeln, J.F., Wiens, D.A., Stein, S., 1986. Mechanisms and depths of atlantic transform earthquakes. J. Geophys. Res. 91, 548–577.

Fornari, D.J., Gallo, D.G., Edwards, M.H., Madsen, J.A., Perfit, M.R., Shor, A.N., 1989. Structure and topography of the Siqueiros transform fault system : Evidence for the development of intra-transform spreading centers. Marine Geophys. Res. 11, 263–299.

Gaina, C., Müller, D., 2007. Cenozoic tectonic and depth/age evolution of the indonesian gateway and associated back-arc basins. Earth Sci. Rev. 83, 177–203. doi:10.1016/j.earscirev.2007.04.004.

Gleason, G., Tullis, J., 1995. A flow law for dislocation creep of quartz aggregates determined with the molten salt cell. Tectonophysics 247, 1–23.

Gurnis, M., Hall, C., Lavier, L., 2004. Evolving force balance during incipient subduction. Geochem. Geophys. Geosyst. 5. doi:10.1029/2003GC000681. doi:10.1029/2003GC000681.

Hall, C., Gurnis, M., 2003. Catastrophic initiation of subduction following forced convergence across fra ctures zones. Earth Planet. Sci. Lett. 212, 15–30. doi:10.1016/S0012-821X(03)00242-5.

Hamai, L., Petit, C., Le Pourhiet, L., Yelles-Chaouche, A., Déverchère, J., Beslier, M.O., Abtout, A., 2018. Towards subduction inception along the inverted north african margin of algeria? insights from thermo-mechanical models. Earth and Planetary Science Letters 501, 13–23. doi:10.1016/j.epsl.2018.08.028.

Hassani, R., Jongmans, D., Chéry, J., 1997. Study of plate deformation and stress in subduction processes using two-dimensional numerical models. J. Geophys. Res. 102, 17951–17965.

Hegarty, K.A., Weissel, J.K., Hayes, D.E., 1983. Convergence at the Caroline-Pacific Plate Boundary: Collision and Subduction. American Geophysical Union (AGU). chapter 18. pp. 326–348. URL: https://agupubs.onlinelibrary.wiley.com/doi/abs/10.1029/GM027p0326, doi:10.1029/GM027p0326,

Karato, S.i., Barbot, S., 2018. Dynamics of fault motion and the origin of contrasting tectonic style between earth and venus. Scientific Reports 8, 1–11. doi:10.1038/s41598-018-30174-6.

Kohli, A., Wolfson-Schwehr, M., Prigent, C., Warren, J.M., 2021. Oceanic transform fault seismicity and slip mode influenced by seawater infiltration. Nat. Geosci. 14, 606–611. doi:10.1038/s41561-021-00778-1.

Kohli, A.H., Warren, J.M., 2020. Evidence for a deep hydrologic cycle on oceanic transform faults. J. Geophys. Res. 125, e2019JB017751. URL: https://agupubs.onlinelibrary.wiley.com/doi/abs/10.1029/2019JB017751, doi:https://doi.org/10.1029/2019JB017751, e2019JB017751 2019JB017751.

Lallemand, S., Arcay, D., 2021. Subduction initiation from the earliest stages to self-sustained subduction: Insights from the analysis of 70 cenozoic sites. Earth-Science Reviews 221, 103779. doi:10.1016/j.earscirev.2021.103779.

Leng, W., Gurnis, M., 2015. Subduction initiation at relic arcs. Geophys. Res. Lett. 42, 7014–7021.

Li, Y., Gurnis, M., 2022. A simple force balance model of subduction initiation. Geophysical Journal International 232, 128–146. doi:10.1093/gji/ggac332.

McGuire, J.J., Collins, J.A., Gouédard, P., Roland, E., Lizarralde, D., Boettcher, M.S., Behn, M.D., Van Der Hilst, R.D., 2012. Variations in earthquake rupture properties along the gofar transform fault, east pacific rise. Nat. Geosci. 5, 336–341. doi:10.1038/NGEO1454.

Mckenzie, D., 1977. The Initiation of Trenches. American Geophysical Union (AGU). pp. 57–61. URL: https://agupubs.onlinelibrary.wiley.com/doi/abs/10.1029/ME001p0057, doi:10.1029/ME001p0057,

McKenzie, D., Jackson, J., Priestley, K., 2005. Thermal structure of oceanic and continental lithosphere. Earth Planet. Sci. Lett. 233, 337–349.

Meckel, T., Mann, P., Mosher, S., Coffin, M., 2005. Influence of cumulative convergence on lithospheric thrust fault development and topography along the australian-pacific plate boundary south of new zealand. Geochem. Geophys. Geosyst. 6. doi:10.1029/2005GC000914.

Meckel, T.A., Coffin, M.F., Mosher, S., Symonds, P., Bernardel, G., Mann, P., 2003. Underthrusting at the hjort trench, australian-pacific plate boundary: Incipient subduction? Geochemistry, Geophysics, Geosystems 4. URL: https://agupubs.onlinelibrary.wiley.com/doi/abs/10.1029/2002GC000498, doi:https://doi.org/10.1029/2002GC000498,

Oxburgh, E., Parmentier, E., 1977. Compositional and density stratification in oceanic lithosphere-causes and consequences. Journal of the Geological Society 133, 343–355.

Peacock, S., Hyndman, R., 1999. Hydrous minerals in the mantle wedge and the maximum depth of subduction thrust earthquakes. Geophys. Res. Lett. 26, 2517–2520.

Ranalli, G., Murphy, D., 1987. Rheological stratification of the lithosphere. Tectonophysics 132, 281–295.

Ren, Y., Geersen, J., Grevemeyer, I., 2022. Impact of spreading rate and age-offset on oceanic transform fault morphology. Geophys. Res. Lett. 49, e2021GL096170. doi:https://doi.org/10.1029/2021GL096170. e2021GL096170 2021GL096170.

Ribe, N., Christensen, U., 1994. Three-dimensional modeling of plume-lithosphere interaction. J. Geophys. Res. 99, 699–682.

Roland, E., Lizarralde, D., McGuire, J.J., Collins, J.A., 2012. Seismic velocity constraints on the material properties that control earthquake behavior at the quebrada-discovery-gofar transform faults, east pacific rise. J. Geophys. Res. 117. doi:10.1029/2012JB009422.

Schellart, W., 2004. Quantifying the net slab pull force as a driving mechanism for plate tectonics. Geophys. Res. Lett. 31. doi:10.1029/2004GL019528.

Thielmann, M., Kaus, B.J.P., 2012. Shear heating induced lithospheric-scale localization: does it result in subduction? Earth Planet. Sci. Lett. 359/360. URL: https://doi.org/10.1016/j.epsl.2012.10.002, doi:10.1016/j.epsl.2012.10.002.

Toth, J., Gurnis, M., 1998. Dynamics of subduction initiation at preexisting fault zones. J. Geophys. Res. 103, 18053–18067.

Turcotte, D., Schubert, G., 1982. Geodynamics: Applications of continuum physics to geological problems. Second ed., Cambridge University Press, New York.

Wang, X., Cao, L., Zhao, M., Cheng, J., He, X., 2022a. What conditions promote atypical subduction: Insights from the Mussau Trench, the Hjort Trench, and the Gagua Ridge. Gond. Res. doi:10.1016/j.gr.2022.10.014.

Wang, Z., Singh, S.C., Prigent, C., Gregory, E.P., Marjanović, M., 2022b. Deep hydration and lithospheric thinning at oceanic transform plate boundaries. Nat. Geosci. , 1–6doi:https://doi.org/10.1038/s41561-022-01003-3.

Weissel, J.K., Anderson, R.N., 1978. Is there a Caroline plate? Earth Planet. Sci. Lett. 41, 143–158.

Wolfson-Schwehr, M., Boettcher, M.S., McGuire, J.J., Collins, J.A., 2014. The relationship between seismicity and fault structure on the discovery transform fault, east pacific rise. Geochem. Geophys. Geosyst. 15, 3698–3712. URL: https://agupubs.onlinelibrary.wiley.com/doi/abs/10.1002/2014GC005445, doi:10.1002/2014GC005445,

Wolfson-Schwehr, M., Boettcher, M.S., 2019. Global characteristics of oceanic transform fault structure and seismicity, in: Transform plate boundaries and fracture zones. Elsevier, pp. 21–59. doi:10.1016/B978-0-12-812064-4.00002-5.

Wu, B., Conrad, C.P., Heuret, A., Lithgow-Bertelloni, C., Lallemand, S., 2008. Reconciling strong slab pull and weak plate bending: The plate motion constraint on the strength of mantle slabs. Earth and Planetary Science Letters 272, 412–421. doi:10.1016/j.epsl.2008.05.009.

Yu, Z., Singh, S.C., Gregory, E.P., Maia, M., Wang, Z., Brunelli, D., 2021. Semibrittle seismic deformation in high-temperature mantle mylonite shear zone along the romanche transform fault. Science Advances 7, eabf3388. doi:10.1126/sciadv.abf3388.

Zhang, G., Zhang, J., Dalton, H., Phillips, D., 2022. Geochemical and chronological constraints on the origin and mantle source of Early Cretaceous arc volcanism on the Gagua Ridge in western Pacific. Geochem., Geophys., Geosyst. 23, e2022GC010424.

Zhang, L., Zlotnik, S., Li, C.F., 2021. Anomalous subduction initiation: young under old oceanic lithosphere. Geochemistry, Geophysics, Geosystems 22, e2020GC009549. doi:10.1029/2020GC009549.

Zhong, X., Li, Z.H., 2019. Forced subduction initiation at passive continental margins: velocity-driven versus stress-driven. Geophys. Res. Lett. 46, 11054–11064. URL: https://agupubs.onlinelibrary.wiley.com/doi/abs/10.1029/2019GL084022, doi:10.1029/2019GL084022,

Zhong, X., Li, Z.H., 2023. Compression at strike-slip fault is a favorable condition for subduction initiation. Geophys. Res. Lett. 50, e2022GL102171. doi:10.1029/2022GL102171.

Zhou, X., Wada, I., 2022. Effects of elasticity on subduction initiation: Insight from 2-d thermomechanical models. Journal of Geophysical Research: Solid Earth , e2022JB024400doi:10.1029/2022JB024400.